

Exploring the transport properties of polytypic and twin-plane nanowires: from tunneling phase-time to spin-orbit interaction effects

M. Rebello Sousa Dias,¹ L. Villegas-Lelovsky,² L. Diago-Cisneros,³ L. K. Castelano,¹ D. F. Cesar,¹ G. E. Marques,¹ and V. Lopez-Richard¹

¹*Departamento de Física, Universidade Federal de São Carlos, 13565-905 São Carlos, SP, Brazil*

²*Instituto de Física, Universidade de Brasília, 70910-900, Brasília, DF, Brazil*

³*Facultad de Física, Universidad de La Habana, Cuba*

(Dated: March 19, 2015)

Abstract

The variety of nanowire crystal structures gave rise to unique and novel transport phenomena. In particular, we have explored the superlattice profile generated by strain field modulation in twin-plane nanowires for the tuning of transport channels and the built-in spin-orbit potential profile of polytypic nanowires, in order to realize a spin filter. The Multicomponent Scattering Approach has been used in terms of the Transfer Matrix Method to describe the phase-time of charge carriers. This system showed advantages for attaining conditions for the propagation of wave packets with negative group velocity. Moreover, the spin transport effect of a potential profile with volumetric spin-orbit bulk inversion asymmetry, as present on polytypic nanowires, was described through the Reverse Runge-Kutta Method. Using the peculiar symmetry of the excited states we have characterized a dominant spin dependence on structural parameters that results in effective spin filtering.

I. INTRODUCTION

The integration of nanowire (NW) architecture as a building-block for electronic and photonic applications has become an issue of considerable research interest.^{1,2} Therefore, the study of their transport properties is a central task for both theoretical and experimental endeavors boosted by the developments of growth techniques that allow minute electronic structure engineering. The ability of thorough control of NW crystal structures by varying parameters as growth temperature and pressure, NW diameter and surface density, precursor molar fraction, III/V aspect ratio, and incorporation of impurity atoms allows the fabrication of a variety of high quality wires displaying zinc-blende, twin-planes (Fig. 1(a)), stacking faults (Fig. 1(d)), and wurtzite crystalline structures.^{3–6} The improving of this level of control can lead to a variety of electronic behaviors and these new prospects have opened different opportunities for the tuning of their transport properties.

The effect of volumetric spin-orbit (SO) bulk inversion asymmetry (BIA) in wires with zincblende crystalline structure has been previously discussed,⁷ where the degeneracy of spin states for each Bloch wavevector k , in the absence of an inversion center, is broken. This leads to the spin splitting of energy states of both electrons and holes without lifting the Kramer degeneracy in the absence of an external magnetic field. It was shown that, although the ground state of a cylindrical NW is always doubly degenerate in terms of the spin polarization at any value of k_z , regardless of the direction, different terms induced by the Dresselhaus SO contribution, split excited levels when considering terms proportional to k_z , the longitudinal component of the wavevector. This is a dominant process that would preserve the spin polarization for small values of k_z opening up the possibility of using transport measurements to explore the preferred spin channels according to the direction of propagation of spin polarized currents along the quasi-1D nanostructures.⁷ In this way and by using the flexibility of manufacturing polytypic nanowire (PNW) structures, we developed transport simulations in a NW presenting regions with and without centers of bulk inversion asymmetry that act as spin scatterers. Thus, if carriers are injected along the z -axis of a PNW with certain incident energy, the peculiar symmetry of excited states in the zincblende cylindrical NW region allows only the transmission of a high degree of spin-polarized current according to the propagation direction. A dominant spin-up or spin-down character of the current depends on the sign of k_z and the current density is directly linked to the interplay

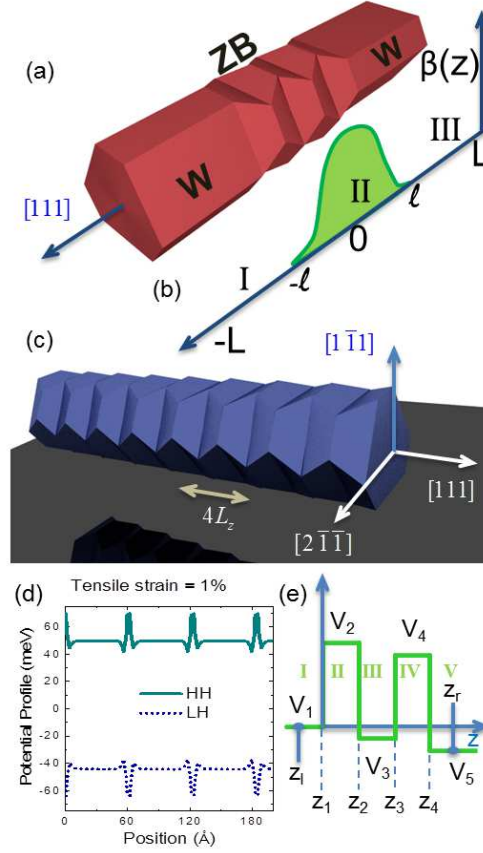


FIG. 1. (a) Schematic diagram of a polytypic nanowire (PNW). (b) Electronic structure profile of a PNW used in the simulation of the spin transport properties, where $\beta(z)$ is the Dresselhaus or BIA spin-orbit potentials. (c) Schematic diagram of a twin-plane nanowire (TPNW) used in our simulation for the electronic structure. (d) Electronic structure profile of the top-most valence subbands. (e) Notation used to characterize the scattering potential profile. The segment $[z_L, z_R]$ represents the periodic cell⁹ for the traveling modes.

between the wire radius and the wavevector.

Likewise, motivated by the successful confirmation of surface effects on transparency modulation of 1D twin-plane based superlattices (TWPSL), the Multicomponent Scattering Approach (MSA)^{8,9} was applied to model and prescribe appealing tunneling events for both uncoupled light-(lh) and heavy-holes (hh) through these NWs. Phase-time calculations show several anomalous transport properties for each kind of charge carriers and reflect, as expected, the mini-band spectrum for 1D-TWPSL.¹⁰ For instance, a clear hallmark of negative values of the phase time will be described. Undoubtedly, such evidences are known

and were reported before for electrons, holes, and twin-photons in typical *III* – *V* layered structures^{11–15} but, as far as we know, they are novel events for TWPSL wires. Additionally, under certain circumstances, oscillating regions were detected for both carriers as they trespass the *n* barriers of the 1D-TWPSLs. This slightly recalls the Ramsauer-Townsend effect.^{9,16,17}

By heeding these two guidelines, the rest of the paper is organized as follows. The next two sections present the theoretical methods used to tackle the transport simulations through spin-orbit interaction centers and twin-planes lattices. Afterwards, the main results are presented followed by the concluding remarks.

II. DRESSELHAUS SPIN-ORBIT EFFECT IN POLYTYPIC NANOWIRES

We simulate various transport properties in a NW presenting regions with and without centers of inversion asymmetry (BIA) introduced by the Dresselhaus SO potential as sketched in Fig. 1 (a). The wavevector has to be considered as an operator which fulfills the temporal inversion symmetry and the single-particle Hamiltonian for the conduction band of a NW, including Dresselhaus SO interaction (SOI), can be written as $\mathcal{H} = \mathcal{H}_0 + \mathcal{H}_D$, where $\mathcal{H}_0 = [\hbar^2 \hat{\mathbf{k}}^2 / 2m^* + V(\mathbf{r}, z)]I$ is the Hamiltonian for uncoupled spin-up and spin-down states, I is the 2×2 identity matrix, and $V(\mathbf{r}, z)$ is the total spatial confinement with lateral $\mathbf{r} = (x, y)$ and longitudinal z along the wire axis for the set of cartesian coordinates. The effective BIA Hamiltonian can be separated into three contributions,

$$\mathcal{H}_D = \mathcal{E}_0 a^3 \begin{pmatrix} \mathcal{H}_{2D} & \mathcal{H}_{1D} + \mathcal{H}_{3D} \\ \mathcal{H}_{1D}^\dagger + \mathcal{H}_{3D}^\dagger & -\mathcal{H}_{2D} \end{pmatrix}, \quad (1)$$

where $\mathcal{H}_{1D} = -\gamma_D \hat{k}_z^2 \hat{k}_-$, $\mathcal{H}_{2D} = -\frac{1}{2} \gamma_D \hat{k}_z (\hat{k}_-^2 + \hat{k}_+^2)$, and $\mathcal{H}_{3D} = -\frac{1}{8} \gamma_D \left\{ \hat{k}_+, (\hat{k}_+^2 - \hat{k}_-^2) \right\}$. They are, respectively, the linear, the quadratic, and the cubic Dresselhaus SOI contributions written in terms of operators \hat{k}_\pm multiplied by the dimensionless parameter $\tilde{\gamma} = \gamma_D / (a^3 \mathcal{E}_0)$, and with $\mathcal{E}_0 = \hbar^2 / (2m^* a^2)$ being the energy scale for the NW confinement inside the cylindrical region. The Schrödinger equation for \mathcal{H} is separable in the entire level spectrum as a product of purely in-plane localized function of the radial coordinate \mathbf{r} times the free motion function along the z -axis, and can be written as,

$$\begin{pmatrix} (\mu_s^2 - \frac{\partial^2}{\partial z^2})\delta_{ss'} + ih_{ss'}\beta(z)\frac{\partial}{\partial z} & -j_{s,s'}^+\beta(z) + g_{ss'}^-\beta(z)\frac{\partial^2}{\partial z^2} \\ -j_{s,s'}^-\beta(z) + g_{ss'}^+\beta(z)\frac{\partial^2}{\partial z^2} & (\mu_s^2 - \frac{\partial^2}{\partial z^2})\delta_{ss'} - ih_{ss'}\beta(z)\frac{\partial}{\partial z} \end{pmatrix} \begin{pmatrix} f_{\alpha\alpha}^{ss'}(z) \\ f_{\alpha'\alpha}^{ss'}(z) \end{pmatrix} = \begin{pmatrix} E & 0 \\ 0 & E \end{pmatrix} \begin{pmatrix} f_{\alpha\alpha}^{ss'}(z) \\ f_{\alpha'\alpha}^{ss'}(z) \end{pmatrix} \quad (2)$$

Here, the index s represents the set of quantum numbers (n, m) , ordered by increasing values of energy $(E_{n,m})$ with $\mu_{n,m} = \sqrt{(E_0/\mathcal{E}_0 - a^2 k_z^2)}$ being the m^{th} -zero of the n^{th} -order Bessel function, $J_n(\mu_{n,m}) = 0$, and with the index α accounting for the spin-up and spin-down states. The innermost matrix elements are $g_{ss'}^\pm = \langle s | \hat{k}_\pm | s' \rangle$, $h_{ss'} = \frac{1}{2} \langle s | \hat{k}_+^2 + \hat{k}_-^2 | s' \rangle$, and $j_{s,s'}^\pm = \frac{1}{8} \langle s | \{ \hat{k}_\pm^2, (\hat{k}_+^2 - \hat{k}_-^2) \} | s' \rangle$. The Dresselhaus coefficient, as function of position along the wire axis, can be emulated as

$$\beta(z) = \frac{\tilde{\gamma}}{2\text{erf}(\ell)} [\text{erf}(z + \ell) - \text{erf}(z - \ell)], \quad (3)$$

where $\text{erf}(z)$ is the error function and 2ℓ is the width of the resulting quasi square region with finite first derivative, illustrated in Fig. 1 (b). Note that the method presented here can afford any kind of potential regardless its spatial shape. After symmetrization of the Dresselhaus Hamiltonian, in the dimensionless form, one reaches a nonlinear set of equations, written as

$$\begin{aligned} & -f_{\alpha\alpha}''^{ss'}(z) + i\beta(z)\tilde{h}f_{\alpha\alpha}'^{ss'}(z) + \beta(z)\tilde{g}^-f_{\alpha\alpha}''^{ss'}(z) \\ & + \beta'(z)\tilde{g}^-f_{\alpha\alpha}'^{ss'}(z) = (k^2 + \mu_s^2)f_{\alpha\alpha}^{ss'}(z) \\ & - \frac{1}{2} \left(i\beta'(z)\tilde{h}f_{\alpha\alpha}^{ss'}(z) + (\beta''(z)\tilde{g}^- + 2\tilde{j}^+\beta(z))f_{\alpha\alpha}^{ss'}(z) \right) \end{aligned} \quad (4)$$

and

$$\begin{aligned} & -f_{\alpha'\alpha}''^{ss'}(z) - i\beta(z)\tilde{h}f_{\alpha'\alpha}'^{ss'}(z) + \beta(z)\tilde{g}^+f_{\alpha'\alpha}''^{ss'}(z) \\ & + \beta'(z)\tilde{g}^+f_{\alpha'\alpha}'^{ss'}(z) = (k^2 + \mu_s^2)f_{\alpha'\alpha}^{ss'}(z) \\ & + \frac{1}{2} \left(i\beta'(z)\tilde{h}f_{\alpha'\alpha}^{ss'}(z) - (\beta''(z)\tilde{g}^+ - 2\tilde{j}^-\beta(z))f_{\alpha'\alpha}^{ss'}(z) \right), \end{aligned} \quad (5)$$

where $k = ak_z$, $\tilde{g}^\pm = ag_{ss'}^\pm$, $\tilde{h} = a^2h_{ss'}$ and $\tilde{j}^\pm = a^3j_{ss'}^\pm$. In order to solve this set of equations we have used the Reverse Runge-Kutta method as shortly described below.

A. Reverse Runge-Kutta

For two spin channels and a single subband $s = s'$, one can write the wavefunction in each of the three regions delimited in Fig. 1 (b) as,

$$\Psi_I = \begin{pmatrix} e^{-izk} R_{\alpha\alpha} + e^{izk} \\ e^{-izk} R_{\alpha'\alpha} \end{pmatrix},$$

$$\Psi_{II} = \begin{pmatrix} \psi_{\alpha\alpha} \\ \psi_{\alpha'\alpha} \end{pmatrix}, \text{ and } \Psi_{III} = \begin{pmatrix} e^{izk} T_{\alpha\alpha} \\ e^{izk} T_{\alpha'\alpha} \end{pmatrix},$$

respectively. From the right interface boundary condition, $\Psi_{II}(L) = \Psi_{III}(L)$, one can write

$$F_{III}(L) = \begin{pmatrix} \frac{\psi_{\alpha\alpha}(L)}{T_{\alpha\alpha}} \\ \frac{\psi_{\alpha'\alpha}(L)}{T_{\alpha'\alpha}} \end{pmatrix} \equiv \begin{pmatrix} e^{izk} \\ e^{izk} \end{pmatrix}, \text{ and}$$

$$F_{II}(z) = \begin{pmatrix} f_{\alpha\alpha}^{ss}(z) \\ f_{\alpha'\alpha}^{ss}(z) \end{pmatrix} \equiv \begin{pmatrix} \frac{\psi_{\alpha\alpha}(z)}{T_{\alpha\alpha}} \\ \frac{\psi_{\alpha'\alpha}(z)}{T_{\alpha'\alpha}} \end{pmatrix},$$

where F_i is the dispersion region function. Hence, $F_{II}(L) = F_{III}(L)$, and $F'_{II}(L) = F'_{III}(L)$ are, respectively,

$$\begin{pmatrix} f_{\alpha\alpha}^{ss}(L) \\ f_{\alpha'\alpha}^{ss}(L) \end{pmatrix} = \begin{pmatrix} e^{iLk} \\ e^{iLk} \end{pmatrix}, \text{ and } \begin{pmatrix} f'_{\alpha\alpha}(L) \\ f'_{\alpha'\alpha}(L) \end{pmatrix} = \begin{pmatrix} ie^{iLk}k \\ ie^{iLk}k \end{pmatrix}. \quad (6)$$

Following the reversal procedure for the left boundary condition, where $\Psi_I(-L) = \Psi_{II}(-L)$, one can address the unknown function F_I as,

$$F_I(-L) = \begin{pmatrix} \frac{\psi_{\alpha\alpha}(-L)}{T_{\alpha\alpha}} \\ \frac{\psi_{\alpha'\alpha}(-L)}{T_{\alpha'\alpha}} \end{pmatrix}, \text{ and}$$

$$F_I(z) = \begin{pmatrix} \frac{e^{izk} R_{\alpha\alpha} + e^{-izk}}{T_{\alpha\alpha}} \\ \frac{e^{izk} R_{\alpha'\alpha}}{T_{\alpha'\alpha}} \end{pmatrix}.$$

Therefore, from the left boundary condition, $F_I(-L) = F_{II}(-L)$, and $F'_I(-L) = F'_{II}(-L)$, along with the current conservation, $|T_{\alpha\alpha}(k)|^2 + |R_{\alpha\alpha}(k)|^2 + |T_{\alpha'\alpha}(k)|^2 + |R_{\alpha'\alpha}(k)|^2 = 1$, one is able to define the transmission (T) and reflection (R) coefficients in terms of the spin components. Thus,

$$T_{\alpha\alpha}(k) = \frac{2k}{kf_{\alpha\alpha}^{ss}(-L) - if'_{\alpha\alpha}{}^{ss}(-L)}, \quad (7)$$

$$R_{\alpha\alpha}(k) = \frac{k f_{\alpha\alpha}^{ss}(-L) + i f'_{\alpha\alpha}{}^{ss}(-L)}{k f_{\alpha\alpha}^{ss}(-L) - i f'_{\alpha\alpha}{}^{ss}(-L)}, \quad (8)$$

$$T_{\alpha'\alpha}(k) = k \sqrt{\frac{1 - |R_{\alpha\alpha}(k)|^2 - |T_{\alpha\alpha}(k)|^2}{k^2 + |f_{\alpha'\alpha}^{ss}(-L)|^2}}, \text{ and} \quad (9)$$

$$R_{\alpha'\alpha}(k) = \sqrt{\frac{1 - |R_{\alpha\alpha}(k)|^2 - |T_{\alpha\alpha}(k)|^2}{k^2 + |f_{\alpha'\alpha}^{ss}(-L)|^2}} \left| f'_{\alpha'\alpha}{}^{ss}(-L) \right| \quad (10)$$

where the $f(-L)$ is obtained employing the right boundary conditions, Eq. (6), along with the z -component Schrödinger Eqs. (4) and (5). Similar expressions are obtained extending this method for multiple subbands.

III. PHASE-TIME IN TWIN-PLANE SUPERLATTICES

In turn, for the simulation of the tunneling properties in the twin plane NW we have used the transfer matrix framework assuming a 1D-TWSL, represented in Fig. 1(c) with alternated layers whose quantum heterogeneity, due to strain field modulation, is revealed along the z -axis in Fig. 1(d). The envelope function (EF) coefficients at both TWSL extremal slabs, are bounded as

$$\begin{bmatrix} A_1 \\ B_1 \end{bmatrix} = \mathbf{M}_1(z_0)^{-1} \cdot \mathbf{M}_2(z_2) \dots \mathbf{M}_4(z_4)^{-1} \cdot \mathbf{M}_5(z_4) \begin{bmatrix} A_5 \\ B_5 \end{bmatrix}, \quad (11)$$

being

$$\mathbf{M}_i = \begin{pmatrix} e^{ik_i z_i} & e^{-ik_i z_i} \\ w_i e^{ik_i z_i} & i v_i e^{-ik_i z_i} \end{pmatrix},$$

the transfer matrix. The EF is given by

$$\Psi_i(z) = A_i e^{ik_i z_i} + B_i e^{-ik_i z_i}, \quad (12)$$

and its weighted derivative, as

$$\frac{1}{m_i} \Psi_i p(z) = \frac{ik_i}{m_i} (A_i - B_i), \quad (13)$$

at both layers I and V of the 1D-TWPSL. [see Fig. 1(d)]. The boundary conditions for scattering quantities can be set by assuming an impinging mixing-free particle (quasi-particle) traveling from the left layer I , represented in Fig. 1(d),

$$\begin{cases} A_1 = 1 & ; & B_1 = T \\ A_5 = R & ; & B_5 = 0 \end{cases}, \quad (14)$$

where T and R stand for transmission and reflection amplitudes, respectively. Next, we establish a correlation between quantities (11) and (14), as

$$\begin{aligned} \begin{bmatrix} 1 \\ R \end{bmatrix} &= \mathbf{M}(z_l, z_r) \cdot \begin{bmatrix} T \\ 0 \end{bmatrix} = \\ &\begin{pmatrix} M_{11}(z_l, z_r) & M_{12}(z_l, z_r) \\ M_{21}(z_l, z_r) & M_{22}(z_l, z_r) \end{pmatrix} \cdot \begin{bmatrix} T \\ 0 \end{bmatrix}, \end{aligned} \quad (15)$$

which straightforwardly lead us to

$$\begin{aligned} T_{ij} &= T_{\Re_{ij}} + \imath T_{\Im_{ij}} = [M_{11}(z_l, z_r)]^{-1} \\ R_{ij} &= R_{\Re_{ij}} + \imath R_{\Im_{ij}} = \frac{M_{21}(z_l, z_r)}{M_{11}(z_l, z_r)}, \end{aligned} \quad (16)$$

the amplitude matrices for transmission and reflection, respectively. Next, we obtain from $|T_{ij}|^2$ and $|R_{ij}|^2$ the scattering probabilities for the transmitted and reflected fluxes, respectively. For the calculation of the tunneling phase-time, a simple procedure is followed. Firstly, we calculated the transmission phase

$$\begin{aligned} \theta_{ij} &= \arctan \left\{ \frac{T_{\Im_{ij}}}{T_{\Re_{ij}}} \right\} + \frac{\pi}{2} \left(1 - \frac{T_{\Re_{ij}}}{|T_{\Re_{ij}}|} \right) = \\ &\arctan \left\{ \frac{\Im(M_{11}(z_l, z_r))}{\Re(M_{11}(z_l, z_r))} \right\} + \frac{\pi}{2} \left(1 - \frac{\Re(M_{11}(z_l, z_r))}{|\Re(M_{11}(z_l, z_r))|} \right), \end{aligned} \quad (17)$$

and afterwards, we derive the n -cell tunneling phase-time^{9,18} $(\tau_{ij})_n = \hbar \frac{\partial}{\partial \mathcal{E}} \theta_{ij}$, assuming left-incoming particle (quasi-particle)

$$(\tau_{ij})_n = \frac{\hbar \Re^2(T_{n_{ij}})}{\Re^2(T_{n_{ij}}) + \Im^2(T_{n_{ij}})} \left\{ \frac{\partial}{\partial \mathcal{E}} \left[\frac{\Im(T_{n_{ij}})}{\Re(T_{n_{ij}})} \right] \right\}. \quad (18)$$

IV. RESULTS AND DISCUSSION

The formalism developed in Sec. II allows the study of spin transport of PNWs, where changes in the zincblende region width, w , the NW diameter, ϕ , the incident energy, \mathcal{E} , and

the SOI strength, β , can be used as tuning parameters. The presented results correspond to an incident spin polarized current injected on the wurtzite region of a InSb PNW, where $\beta = 760.1 \text{ eV}\cdot\text{\AA}^3$. We will see that the SOI within the zincblende region gives rise to a small net polarization. Projecting it to several sequential regions, it is possible to realize spin filters and modulate the densities of spin-polarized current flowing in both parallel and antiparallel directions of the NW.

In order to characterize the system response to the injection of a spin-unpolarized superposition of spin-up and spin-down currents, we calculate the spin persistence ratio as defined by $[|T_{\alpha\alpha}|^2 + |T_{\alpha'\alpha'}|^2 - (|T_{\alpha'\alpha}|^2 + |T_{\alpha\alpha'}|^2)]/T$, where $T = |T_{\alpha\alpha}|^2 + |T_{\alpha'\alpha'}|^2 + |T_{\alpha'\alpha}|^2 + |T_{\alpha\alpha'}|^2$. Figure 2 shows the color code maps of characteristic persistence vs. incident energy, \mathcal{E} , and w , and vs. \mathcal{E} and ϕ . Note, that the persistence is always positive, while characterizing the transmitted current, but does not reach the unity (Figs. 2 (a) and (c)). This positiveness refers to a signature of almost perfect spin-preserving channel, as expected due to the non-degenerated ground state,⁷ but there are oscillating regions which evolve with changes in \mathcal{E} , w , and ϕ . On the other hand, from the characterized reflected current it is possible to observe that the persistence goes from spin-preserving to spin-reversing (negative values) channels. The spin-reversing regions are identified by negative numbers and also evolve with changes in \mathcal{E} , w , and ϕ . Despite the difference of spin-preserving and spin-reversing channels, the oscillation pattern of the reflection coefficient is doubled in comparison to the transmitted one and this should be expected once the current crosses twice the region of Dresselhaus SOI.¹⁹ Moreover, the evolution of the oscillations goes with both \mathcal{E} and ϕ , so that $\mathcal{E}\phi = \text{constant}$, as shown in panels (c) and (d) of Fig. 2, due to the modulation of the energy levels with ϕ , Eq. (2).

When considering excited states in the transport, one can expect a small net spin polarization for the current. This is due to the fact that for transport along the z -direction, the Dresselhaus SOI will produce the precession of both spin-components but in different ways.⁷ The degree of spin-polarization is defined by $[|T_{\alpha\alpha}|^2 + |T_{\alpha'\alpha'}|^2 - (|T_{\alpha'\alpha}|^2 + |T_{\alpha\alpha'}|^2)]/T$. Figure 3 shows the polarization as function of \mathcal{E} and w in panels (a) and (b), and as a function of \mathcal{E} and ϕ , in panels (c) and (d).

Observe that the transmission displayed in Fig. 3 (a) shows well defined polarization regions which evolve with both \mathcal{E} and w . Around $\mathcal{E} = 5 \text{ meV}$ and $w = 150 \text{ \AA}$, a smaller percentage of spin-down polarization is evident, as well as for $\mathcal{E} = 45 \text{ meV}$. Looking at

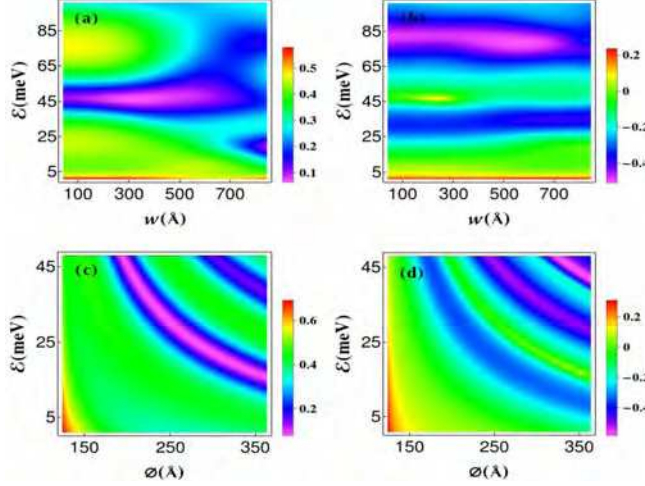


FIG. 2. Persistence contour maps of polytypic InSb quantum wire for the first band where $\beta = 760.1 \text{ eV}\cdot\text{\AA}^3$. Panels (a) and (b) show the transmission and reflection as function of the barrier width and energy for a wire with radius 101 \AA . In panels (c) and (d) we show transmission and reflection as function of the wire diameter and energy.

$w = 800 \text{ \AA}$, one can see an opposite spin-polarization for $\mathcal{E} = 45 \text{ meV}$. Moreover, it is clear that at this width w , a modulation of the polarization takes place, from spin-down to spin-up character, by varying \mathcal{E} . This last hallmark is also revealed in the reflection panel, shown in Fig. 3 (b), but with opposite polarization features. Additionally, Figs. 3 (c) and (d) show the same behavior of Figs. 2 (c) and (d), with oscillations occurring by varying both \mathcal{E} and ϕ , such that $\mathcal{E}\phi = \text{constant}$. These results indicate the possibility of modulation of the polarization by selecting the incident energy of carriers, the NW wire width, the zincblende region width, and the SO potential.

The presented results for the spin persistence and polarization refer only to a configuration of one zincblende region between two wurtzite layers, as seen in Fig. 1 (b), and this was enough to characterize a small percentage of spin flux modulation. Increasing the number of layers containing the zincblende regions, one can expect an increase of the polarization. Figure 4 shows the transmission, (a), and reflection, (b), polarizations for multiple wurtzite/zincblende/wurtzite regions. As can be noted, an increasing number of layers leads to increasing spin filtering and enhancement of the final polarization.

Along with the polytypism, the growth conditions may lead to controlled stacking faults appearance and the synthesis of twin plane superlattices. For these later, as represented

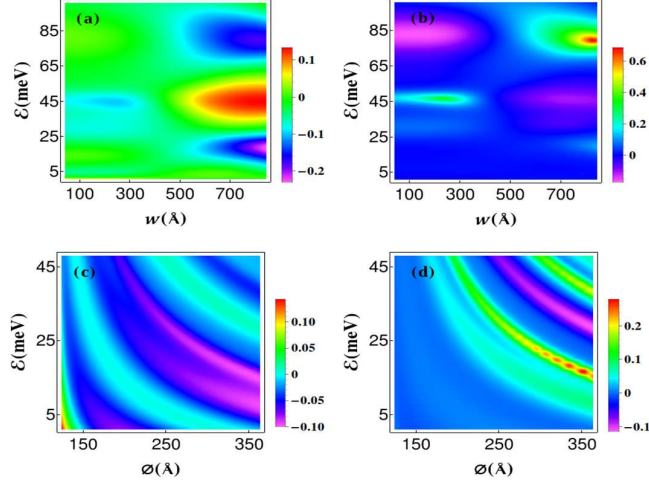


FIG. 3. Polarization contour maps of polytypic InSb NW for the first subband $\beta = 760.1 \text{ eV} \cdot \text{\AA}^3$. Transmission (a) and reflection (b) as function of the barrier width and incident energy for a wire with radius of 101 \AA . Transmission (c) and reflection (d) as function of the wire diameter and incident energy.

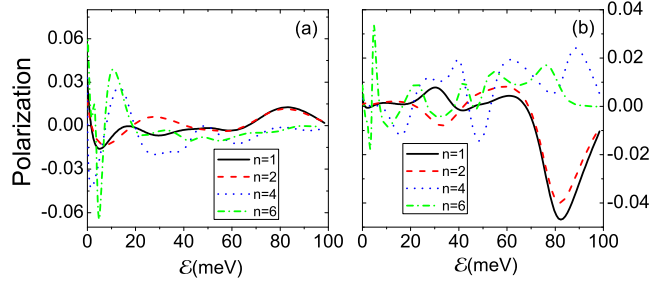


FIG. 4. Polarization of polytypic InSb NW with multiple wurtzite regions, n , where $\beta = 760.1 \text{ eV} \cdot \text{\AA}^3$. (a) Transmission and (b) reflection as function of the energy for a wire with radius of 101 \AA .

in as Fig. 1(c), we have proposed a transport analysis of the tunneling phase-time for both lh and hh. Here, the results for electrons were not shown due to similarities with the lh transport results.¹⁰

Using the formalism of Sec. III, the mini-band spectrum for holes tunneling through ($n = 2 - 100$) 1D-TWPSL is depicted in Fig. 5 as τ_n (18) and evolves with the carrier incident energy, \mathcal{E} . As expected, this simulation agrees with an previous direct calculation of the 1D-TWPSL spectrum¹⁰ and responds to the mini-band spectrum of the 1D-TWPSL, *i.e.* it reproduces accurately the quasi-stationary holes states of the embedded 1D-TWPSL

quantum wells. We found the double resonant tunneling barrier (DBRT) curve ($n = 2$, red dashed line) to represent a lower bound for the 1D-TWPSL mini-band spectrum as had been reported for electrons²⁰ and for holes⁹ in two-dimensional systems (see Fig. 5 (a) and (c)). Appealing regularity for energy sections has been found, where $\tau_{100} < \tau_{30} < \tau_2 < 0$ (see dips in Figs. 5(b) and (d)), where the transmission vanishes and, thereby, coincides with the mini-band forbidden regions of the system (Figs. 5(a) and (c)). In other words, this abnormal behavior for holes is directly connected to a large backscattering ($|T(\mathcal{E})|^2 \simeq 0$).^{11,12,21} The later could be due to the fact that negative values of τ are not only related to the incident wave from left but also might be a combination of both incident and accumulatively reflected waves from the 1D-TWPSL quantum barriers traveling towards the left-hand side.¹² One may notice that the quasi-classical free motion time, $\tau_f = \frac{nL_z m_{eff}}{\hbar k}$, which characterizes the temporal scale for a particle with mass m_{eff} to travel through a none-scattering space region of dimension n times the thickness L_z ,⁹ can be straightforwardly compared with Eq. (18). Indeed, in our case, a striking quality arises whenever $(\tau_f)_{2,30,100} > \tau_{2,30,100}$, for the mini-gap regions, respectively (Fig. 5 (b) and (d)). Therefore, for incoming hh states, with energy in the neighborhood of 20 meV, $(\tau_f)_{100} - \tau_{100} \approx 60$ ps, while for incoming lh with incident energy ~ 120 meV, $(\tau_f)_{100} - \tau_{100} \approx 15$ ps. This earlier arrival time for both hh and lh, previously predicted for electrons²⁰ and holes⁹ that tunnel through a two-dimensional DBRT and a SL, suggests a faster passage of holes trough a 1D-TWPSL, under specific conditions. The regularity of more speedily passage of hh, compared to that of lh,⁹ is clearly preserved in our numerical simulation. Importantly, only at low energies (~ 5 meV for hh, and $\sim [14 - 23]$ meV for lh) τ_{30} approaches $(\tau_f)_{30}$ from upper side down, as detected for electrons²⁰ and holes in two-dimensional SL.⁹ Additionally, it seems to be satisfied that $(\tau_f)_{2,30,100} > \tau_{2,30,100}$ for the rest of impinging energy values in the transparent region, contrary to the two-dimensional case.⁹

In order to spread some light and try to elucidate some features of the negative phase-time (eq. (18)) values, one can see in Fig. 6 the transmission amplitude, $T_{ij} = T_{\Re_{ij}} + i T_{\Im_{ij}}$, in the complex plane for different numbers of cells, n . Here, $\theta_{ij}(\mathcal{E})$ has been taken as the angle and $|T(\mathcal{E})|^2$ as the radius. As can be seen, the major signature of the curves is their clockwise direction evolution, which can be directly related with positive phase-time values. However, counterclockwise segments clearly appear for hh with $n = 3$ (green-triangles) and $n = 4$ (blue-diamonds), characterized by loops in Fig 6(b). Interestingly, these loops seems to be

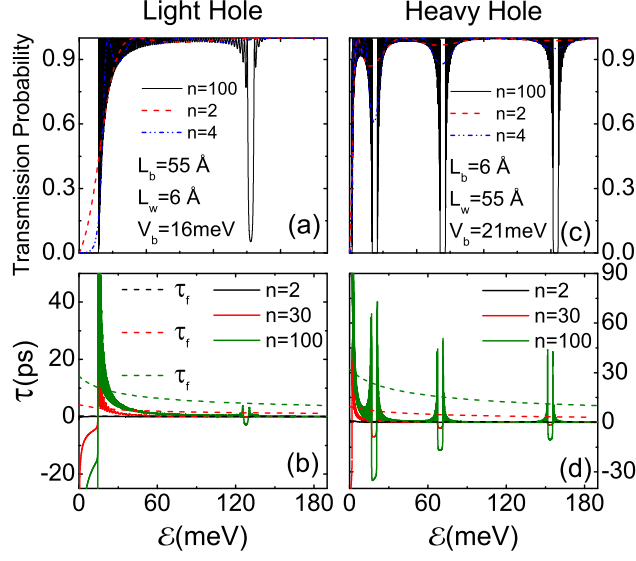


FIG. 5. Calculated transmission probability and phase-time (τ_n) for various sequences of twin-plane cells, n , in a 1D-TWPSL as a function of incident energy (\mathcal{E}): (a) and (b) Transmission probability, τ and quasi-classical free motion time (τ_f), respectively, for light-holes (lh). (c) and (d) Transmission probability, τ and τ_f , respectively, for heavy-holes (hh).

modulated by the $n = 1$ (black-squares) curve as a lower bound, Fig 6(b). The last could be a certain resemblance of a similar average behavior, detected for electrons²⁰ and holes⁹ in two-dimensional systems. The counterclockwise direction of $\theta_{ij}(\mathcal{E})$ is directly related with negative values of the phase-time. For lh, in Fig. 6(a), this occurs when $|T(\mathcal{E})|^2 \simeq 0$ for $n \geq 4$ and for a large number of cells. One can find this negative values of τ for hh when $|T(\mathcal{E})|^2 \simeq 0$ for $n \geq 3$, in Fig. 6(b). Despite some criticism in the specialized literature, clear hallmarks of negative values for τ are reported, where any numerical artifact has been accurately excluded. In spite of the interpretation proposed above, for this counterintuitive topic, a conclusive robust theoretical modeling remains a puzzle. Such evidences are novel events for TWPSL NWs, although they are well established on other systems.^{11–15}

Figures 7(b) and (c) display the calculated τ_n , eq. (18), for different sequences of TWP cells caused by the strain effect, as a function of the barrier width, L_b . Oscillating regions are detected for both hh and lh, as they trespass the $n = 30, 100$ 1D-TWPSLs with low values of energy, $\mathcal{E} < 0.5V_b$ [see Fig. 7 (b), (c), (e), and (f)]. Accumulative barrier interferences with evanescent hole states have been assigned as the possible origin of these oscillations. This slightly recalls the Ramsauer-Townsend effect.⁹ This behavior fades away abruptly at

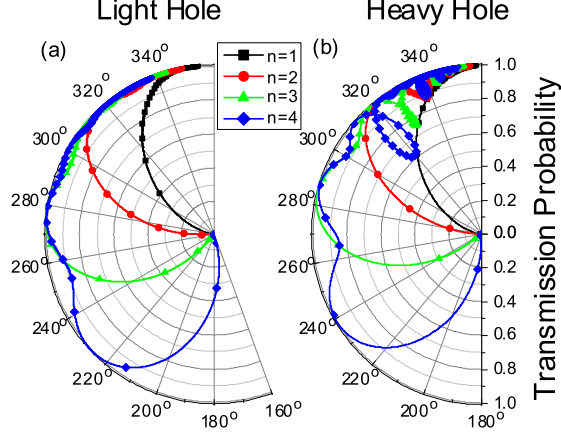


FIG. 6. Representation of the transmission amplitude through different numbers of cells, n : $T_{ij} = T_{\mathcal{R}_{ij}} + iT_{\mathcal{S}_{ij}}$, in the complex plane for increasing incident energy. (a) lh and (b) hh. Note that both diagrams have been rotated for clarity.

$L_b \approx 50$ Å for lh whereas for hh is observed at $L_b \approx 30$ Å. It can be argued that beyond a critical value of barrier width, the wavefunction penetration length becomes negligibly small and, thereby, the $|T(\mathcal{E})|^2$ tends to vanish while $\tau_n < 0$ values arise. None of such oscillations has been found for the DBRT case ($n = 2$).

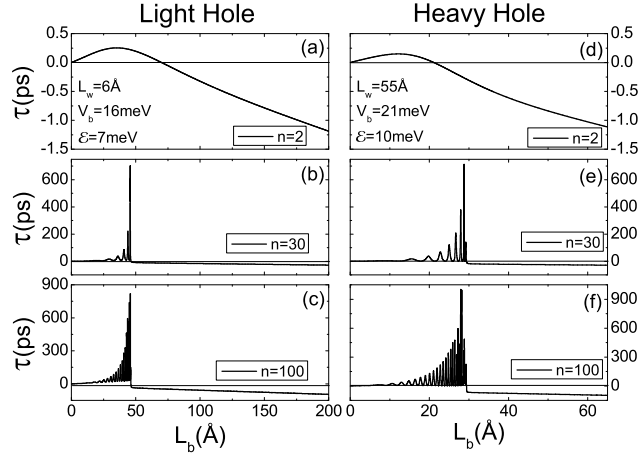


FIG. 7. Calculated τ_n for various sequences of twin-plane cells in a 1D-TWPSL as a function of the barrier width (L_b). For lh: (a), (b), and (c). For hh: (d), (e), and (f).

V. CONCLUSION

In summary, motivated by well established methods for manufacturing polytypic and twin-plane NWs, we have proposed two different carrier transport studies for the characterization of these systems. The first one was the spin transport simulation on a polytypic NW structure presenting regions with (zincblende) and without (wurtzite) Dresselhaus SO potential. For this transport calculation we developed a new approach based on the Reverse Runge-Kutta method. We have found that carries injected with certain energy along the z -axis of a TPNW, would allow the transmission of spin-up current along the $+z$ -direction and spin-down current along the $-z$ -direction, as due to the peculiar symmetry of the excited states in the zincblende cylindrical region. Furthermore, the increasing number of layers in the structure leads to increasing spin filtering ability as well as an enhancement of the final current polarization. The spin-polarized current density can be directly linked to the interplay between the wire radius and width of the Dresselhaus SOI layer.

In turn, the second simulation uses the MSA and TMM methods to study the charge carriers passage through a strained 1D-TWPSL. As expected, the calculation averaged out the mini-band spectrum for 1D-TWPSL. Amplitude oscillating regions were obtained for both hh and lh carrier currents with low values of incident energy, thus evoking the Ramsauer-Townsend effect. Moreover, the phase-time τ_n assumes negative values whenever the 1D-TWPSL properties reach a minimum or negligible transmission probabilities. This abnormal behavior is directly connected to a large carrier backscattering at barrier regions of the finite superlattice.

In order to elucidate this effect, we have characterized the transmission amplitude in the complex plane where the major clockwise signatures were directly related to positive values of τ_n , whereas the minor counterclockwise ones were connected to negative values of the phase-time. This effect is only observed for structures with $n > 2$. We hope that these findings would stimulate further search for the realization of spin filtering structures.

ACKNOWLEDGMENTS

The authors are grateful for financial support by the Brazilian Agencies CNPq, CAPES, FAPESP (Grant # 2012/02655-1), and the Academic Visiting Program of CLAF-PLAF of

the Brazilian Physical Society. L.D-C is grateful for the hospitality of UFSCar Physics Department.

- ¹ C. Thelander, P. Agarwal, S. Brongersma, J. Eymery, L. Feiner, A. Forchel, M. Scheffler, W. Riess, B. Ohlsson, U. Gösele, L. Samuelson, *Mater. Today* **9**, 281735 (2006).
- ² C. M. Lieber, Z. L. Wang, *MRS Bull.* **32**, 99 (2007).
- ³ R. E. Algra, M. A. Verheijen, M. T. Borgström, L.-F. Feiner, G. Immink, W. J. P. van Enkevort, E. Vlieg, E. P. A. M. Bakkers, *Nature*, **456**, 369 (2008).
- ⁴ K. A. Dick, P. Caroff, J. Bolinsson¹, M. E. Messing, J. Johansson, K. Deppert, L. R. Wallenberg, L. Samuelson, *Semicond. Sci. Technol.* **25**, 024009 (2010).
- ⁵ A. T. Vogel, J. de Boor, J. V. Wittemann, S. L. Mensah, P. Werner, V. Schmidt, *Cryst. Growth Des.* **11**, 1896171900 (2011).
- ⁶ P. Caroff, K. A. Dick, J. Johansson, M. E. Messing, K. Deppert and L. Samuelson, *Nature Nanotechnology* **4**, 50 - 55 (2009).
- ⁷ L. Villegas-Lelovsky, C. Trallero-Giner, M. Rebello Sousa Dias, V. Lopez-Richard, G. E. Marques, *Phys. Rev. B* **79**, 155306 (2009).
- ⁸ R. Tsu and L. Esaki, *Appl. Phys. Lett.* **22**, 562 (1973).
- ⁹ S. Arias-Laso and L. Diago-Cisneros, *Physica E* **44**, 1730 (2012).
- ¹⁰ H. Tsuzuki, D. F. Csar, M. Rebello de Sousa Dias, L. K. Castelano, V. Lopez-Richard, J. P. Rino, and G. E. Marques), *ACS Nano* **5**, 5519 (2011).
- ¹¹ R.-M. Vetter, A. Haibel, and G. Nimtz, *Phys. Rev. E* **63**, 046701 (2001).
- ¹² G. Dolling, C. Enkrich, M. Wegener, C. M. Soukoulis, S. Linden, *Science* **312**, 892 (2006).
- ¹³ Li-Gang Wang, Jing-Ping Xu, and Shi-Yao Zhu, *Phys. Rev. E* **70**, 066624 (2004)
- ¹⁴ Xi Chen and Chun-Fang Li, *Eur. Phys. J. B* **46**, 433 (2005)
- ¹⁵ J. G. Muga, I. L. Egusquiza, J. A. Damborenea, and F. Delgado, *Phys. Rev. A* **66**, 042115 (2002).
- ¹⁶ V. A. Bailey and J. S. Townsend, *Philosophical Magazine S. 6* **42** 87317891 (1921).
- ¹⁷ C. Ramsauer, *Annalen der Physik* **64** 51317540 (1921).
- ¹⁸ L. Diago-Cisneros, H. Rodríguez-Coppola, R. Pérez-Álvarez, and P. Pereyra, *Phys. Rev. B* **74**, 045308 (2006).

- ¹⁹ M. Rebello Sousa Dias, V. Lopez-Richard, G. E. Marques, S. Ulloa, EPL **106**, 17002 (2014).
- ²⁰ P. Pereyra, Phys. Rev. Lett. **84**, 1772 (2000)
- ²¹ E. H. Hauge and J. A. Stövneng, Rev. Mod. Phys. **61**, 917 (1989).